Nanoscale Advances

ROYAL SOCIETY OF CHEMISTRY

PAPER

View Article Online
View Journal

Cite this: DOI: 10.1039/d5na00691k

Resource-efficient pre-treatment with partial desalination approach using graphene-MXene coated cellulose filters for desalination plants

Madhusudhana M. Devadiga, [a] Anushree S. Bhat,[a] Subham Sarangi,[a] Anil Kumar H. S.,[b] Nannan Wang [c] and Santosh K. Tiwari *[a]

The impact of the water crisis is significant, and among the available solutions, the desalination of seawater and brackish water stands out. Herein, a simple, energy-efficient, and scalable, dual-functional method for pretreatment followed by partial desalination of seawater is reported. A hybrid filtration setup was employed, consisting of naturally available, environmentally friendly adsorbents such as fine sand, carbon, and cellulose filters coated with graphene oxide (GO) and $Ti_3C_2T_x$ MXene. These materials are arranged in layers forming a sandwich structure, allowing seawater to pass through naturally by gravity, without external pressure, making the system highly energy-efficient. The lab-made hybrid filter can process up to ~2 L of water per hour using a small effective filtration area of ~63 cm^2. The influence of coating concentration was studied using four different concentrations, where 1 mg mL^{-1} coatings showed better performance for both GO and MXene. After filtration, the water was analysed using various quality parameters, and the filter components were examined *via* FESEM with EDS to assess morphology and elemental composition. Among GO and MXene, GO-coated filters performed better, achieving a satisfactory pretreatment and a 17.7% reduction in salinity without any external energy input. The salt rejection is mainly attributed to adsorption and electrostatic interactions between the coated materials and dissolved ions in seawater.

Received 18th July 2025
Accepted 22nd November 2025

DOI: 10.1039/d5na00691k

rsc.li/nanoscale-advances

Introduction

The global water crisis stems from a complex interaction of human and climatic factors, including rapid population growth, inefficient agricultural practices, industrial and domestic pollution, and excessive groundwater extraction, all placing immense pressure on freshwater resources.[1,2] Climate change worsens this by altering hydrological cycles, with shifting precipitation patterns, prolonged droughts, intensified floods, and rapid glacial melt.[1] These impacts contribute to reduced freshwater availability and related challenges.[3] The convergence of these issues highlights the urgent need for sustainable, integrated water management and innovative strategies to guarantee long-term water security. Key solutions to the crisis focus on improved water resource management, such as wastewater reclamation, precision agriculture, and advanced desalination technologies. These approaches aim to optimize water use and reduce human-induced stress on freshwater availability and quality.[3] Among them, desalination has become a leading option, offering a climate-resilient and virtually unlimited freshwater source from saline water. It is especially vital in arid and coastal regions with growing populations and declining traditional supplies.[4] Common desalination technologies include reverse osmosis (RO), forward osmosis (FO), nanofiltration (NF), multistage flash distillation (MSF), multi-effect distillation (MED), membrane distillation (MD), electrodialysis (ED), vapour compression (VC), zero liquid discharge (ZLD), and others.[5] In this regard, RO and thermal processes like MSF and MED are the most widely used.[6,7] Thermal methods tolerate varying feedwater quality but are highly energy-intensive due to water's high latent heat of vaporization (~2260 kJ kg^{-1}), resulting in greater operational costs and emissions.[8] On the other hand, RO, which pushes water through semi-permeable membranes, offers better energy efficiency and operating flexibility but is prone to membrane fouling and demands extensive pretreatment.[9]

Pretreatment is essential for the efficient and sustainable operation of membrane-based systems like RO. It prevents fouling, scaling, and membrane degradation by removing particulates, organic matter, bacteria, and scale-forming ions such as Ca^{2+} and Mg^{2+}. This enhances water flux, salt rejection,

[a]Centre for New Materials and Surface Engineering, Department of Chemistry, NMAM Institute of Technology (NMAMIT), Nitte (Deemed to be University), Nitte, Karnataka, 574110, India. E-mail: ismgraphene@gmail.com

[b]Nitte (Deemed to be University), NMAM Institute of Technology (NMAMIT), Nitte, Department of Biotechnology Engineering, Karkala, Karnataka, 574110, India

[c]State Key Laboratory of Featured Metal Materials and Life-cycle Safety for Composite Structures, School of Resources, Environment and Materials, Guangxi University, Nanning, Guangxi, 530004, China

and membrane lifespan, along with reducing chemical cleaning needs and operating costs.[10,11] Therefore, inadequate pretreatment can lead to faster system degradation, increased energy use, and reduced water recovery. It also compromises water quality and consistency, as discussed elsewhere.[9–11] Thus, operative pretreatment is crucial for both the economic and technical success of RO systems.[12] Pretreatment tactics are categorized into three types: conventional, non-conventional, and hybrid methods.[10] Subcategories for these types are shown in Fig. 1. Different types of commercially available pretreatment techniques are given in Table S1 (see SI) for more insight.

Currently existing RO pretreatment systems face considerable challenges, such as membrane fouling, excessive chemical use, and a lack of adaptability to changing water quality conditions. Fouling induced by organics, biofilms, and particles results in both decreased efficiency and increased maintenance. The use of chemicals raises costs and causes environmental issues, and the inadequate removal of contaminants, such as algae, organic matter and the production of sludge, further impedes sustainability. In recent years, 2D nanomaterials like graphene, MXene, BN nanosheets, MoS_2, *etc.*, have been getting huge attention in water technologies.[13–15] Coating of these 2D materials enhances the performance of the filter/membrane by providing ultrathin, highly conductive, and hydrophilic surfaces with tunable nanochannels that enable precise ion sieving, antifouling behaviour, and improved water flux. Their 2D layered structure warrants rapid mass transfer, mechanical reinforcement, and selective permeability, making them ideal for advanced water treatment, seawater desalination and contaminant removal applications. Li *et al.* incorporated $Ti_3C_2T_x$ MXene into a sodium alginate polymer matrix for the removal of organic dyes and inorganic salts from water, achieving very high-water flux with ≥99.5% dye rejection.[16] Zheng *et al.* fabricated an exceptional self-cleaning MXene-based membrane by vacuum-assisted deposition of MXene dispersion on porous polymeric support for highly efficient oil/water separation. The membrane showed a very high-water flux value of ~2500 L per m^2 per h per bar with >99% oil rejection efficiency.[17] In another study, the *in situ* growth of BIC@MIL-101(Fe) metal organic framework on MXene nanosheets, followed by self-assembly on porous polymeric substrate, was performed by Li *et al.* for oil–water emulsion separation with impressive results.[18] Similarly to this study, Wang *et al.* replaced MXene with GO and studied for similar applications, proving that GO coatings are also an excellent option for water purification and related technologies.[19] Ranieri *et al.* presented solid experimental evidence that gravity-driven membranes are a feasible and ecologically benign alternative to standard seawater reverse osmosis (SWRO) pre-treatment procedures. Its unique capacity to use a stable biofilm for both hydraulic stability and biological organic carbon removal opens the door to more durable, energy-efficient, and chemically sustainable desalination processes.[20] So, it is evident that 2D materials-coated filters are an excellent option for the pretreatment of raw seawater *via* a simple gravity-driven filtration setup.

Herein, we are reporting a facile, green, scalable approach for the pretreatment of seawater using a hybrid filtration setup. We employed naturally available materials with slight modifications to improve their adsorption proficiency, like ball-milled fine sand and functionalized carbon. Normal cellulose filters were modified to tailor their pore size by coating them with GO and $Ti_3C_2T_x$ MXene, which are known for their excellent applications in water technologies owing to their exceptional properties. The GO/MXene-coated cellulose filter can act as an efficient and sustainable medium for seawater pretreatment using a simple gravity-driven filtration process. Unlike conventional GO/MXene-based membranes that depend on pressure-assisted systems or complex fabrication techniques, this method capitalizes on the synergistic properties of these materials, which are uniformly integrated onto a biodegradable cellulose substrate. This configuration is found to be efficient in achieving better pretreatment performance with the added advantage of partial desalination of ~17.7% in a single step.

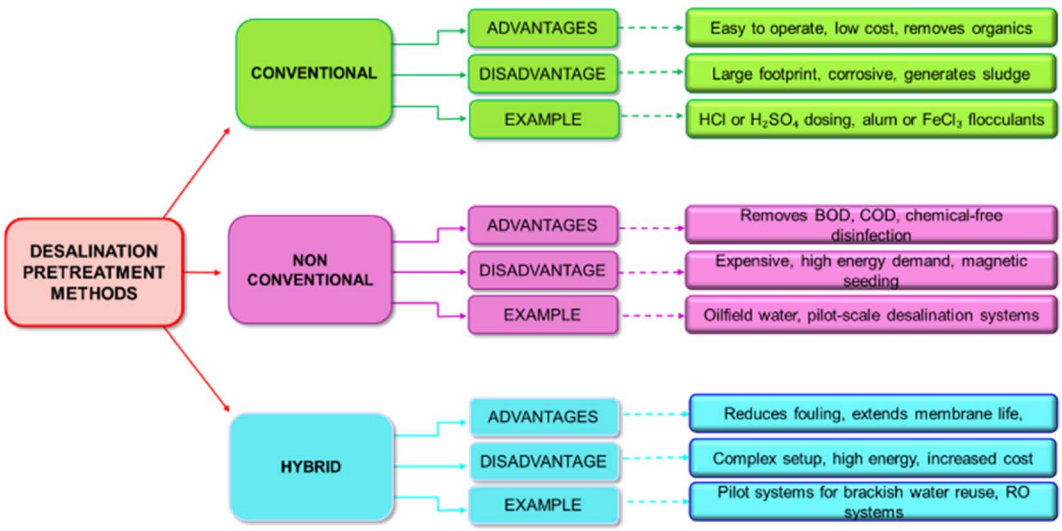

Fig. 1 Major classifications of pretreatment methods for desalination, their merits and demerits, with examples.

Also, the chosen materials in the fabrication of the hybrid filter, energy-efficient working pathway, scalability, and eco-friendliness make the process a promising solution for a sustainable water future.

Materials and methods

For the current study, we have utilized natural graphite, H_2SO_4, H_3PO_4, $KMnO_4$, 30% H_2O_2, HCl, ethanol, Ti_3AlC_2 MAX phase powder, hydrofluoric acid (HF), tetramethyl ammonium hydroxide (TMAOH), cellulose filter paper (Whatman Grade 41), activated carbon, HNO_3 and DI water. All the chemicals were procured from Sigma Aldrich, India, and used directly without any further purifications. The seawater for the study was taken from Padubidri Blue Flag beach, Udupi, India. The necessary instruments, such as weighing balance, thermoagitator, centrifuge machine, spin coater, high-energy planetary ball mill, and vacuum oven available in the laboratory were employed for the synthesis (GO and $Ti_3C_2T_x$ MXene) and fabrication of the coated Whatman filter paper.

Synthesis of GO nanosheets

GO was synthesised using the improved Hummers' method as described in the cited literature.[21,22] Briefly, a mixture of 3 g of natural graphite and 18 g of $KMnO_4$ was added slowly (~3 hours) to a 9 : 1 mixture of H_2SO_4 : H_3PO_4 (360 mL : 40 mL). During this addition, a slight exotherm was observed. Then the reaction mass was heated to 50 °C and stirred for 12 hours at the same temperature. The reaction mass was cooled to room temperature and poured into approximately 400 mL of ice containing 3 mL of 30% H_2O_2. The mixture was then filtered through polyester fibre, followed by the centrifuging of the filtrate for 4 hours at 4000 rpm. The supernatant was decanted, and the solid obtained was washed repeatedly with distilled water to remove acid content. Further washed with 30% HCl (200 mL), followed by 200 mL of ethanol (twice). The solid obtained was dried under vacuum overnight.

Synthesis of $Ti_3C_2T_x$ MXene

For the synthesis of $Ti_3C_2T_x$ MXene, a well-established chemical etching method was used as reported in the literature.[23] 40 mL of 40% HF was taken in a plastic beaker. Added 2 g of Ti_3AlC_2 MAX powder to the beaker slowly with intervals of 5 minutes. The reaction mass was stirred at room temperature for 16 hours. Collected the solid using centrifugation and washed repeatedly with DI water to remove HF (until the pH of the supernatant reached 7). The solid obtained was added to 200 mL of DI water containing 2 g of TMAOH as the delaminating agent and stirred for 12 hours at room temperature. The solid was collected by centrifugation and washed with DI water to remove TMAOH (until the basic pH becomes neutral). The solid obtained was dried under vacuum at 120 °C overnight.

Fabrication of GO and $Ti_3C_2T_x$-coated cellulose filters

The schematic representation for the synthesis of GO and MXene, followed by coating them onto the cellulose filter, is represented in Fig. 2. For the coating of GO and MXene, stock solutions of concentration 1 mg mL^{-1} were prepared by dispersing 100 mg of GO and MXene, correspondingly in 100 mL DI water. The solutions were sonicated for 1 hour (interval-based with 10 min ON/OFF). Three different concentrations of 0.25 mg mL^{-1}, 0.50 mg mL^{-1}, and 0.75 mg mL^{-1} were prepared from each stock solution by taking the appropriate quantity of solution and diluting it with DI water. All solutions (including the stock solution) were sonicated for 20 minutes before coating them onto the substrate. A Whatman filter paper (grade 41) was used as the substrate for coating. It was fixed to the sample holder of the spin coater device with the help of surgical tape. A 5 mL syringe was used to slowly add the solution to be coated into the substrate, which was rotating at 1000 rpm. Each face of the filter paper was coated with 5 mL of the solution (a total of 10 mL coating per filter paper) and kept in an oven at 60 °C for 1 hour to remove water from the filter paper. The images of GO and MXene-coated filters with four different concentrations are given in Fig. 3.

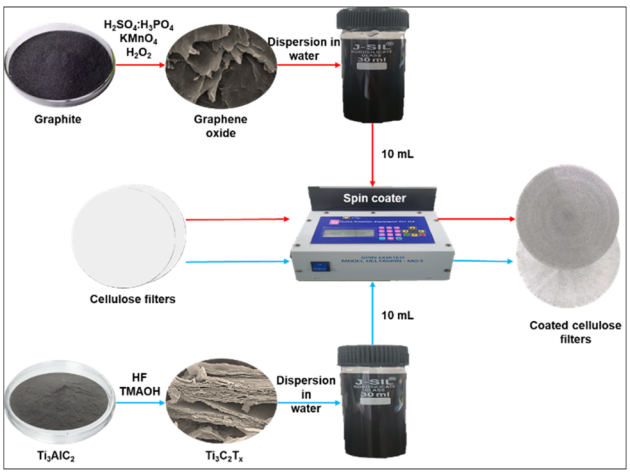

Fig. 2 Schematic representation of the synthesis of GO and MXene followed by coating them onto the cellulose filter using a spin coater device.

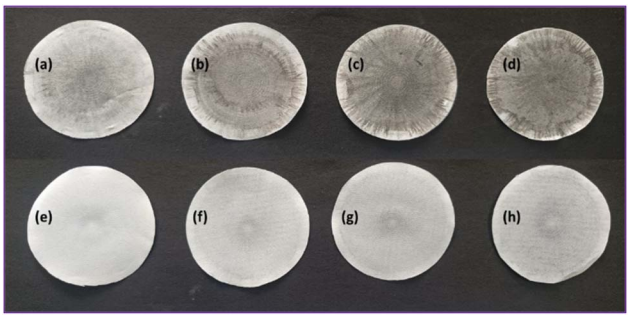

Fig. 3 Digital photographs of cellulose filter paper coated with GO and $Ti_3C_2T_x$ of different concentrations. GO-coated filters with 0.25 (a), 0.50 (b), 0.75 (c) and 1 mg mL^{-1} (d) concentrated solutions and $Ti_3C_2T_x$-coated filters with 0.25 (e), 0.50 (f), 0.75 (g) and 1 mg mL^{-1} (h) concentrated solutions.

Functionalization of activated carbon by acid mixture treatment

Activated carbon itself is one of the best-known adsorbent materials. Treating them with an acid mixture adds several advantages, like enhancement in the adsorption efficiency, high selectivity, improved hydrophilicity, an increase in surface reactivity, *etc.* About 5 g of activated carbon was taken in a round-bottom flask fitted to a thermoagitator. 50 mL of $HNO_3 : H_2SO_4$ (3 : 1) acid mixture was slowly added to the RB. The temperature of the reaction mixture was gradually raised to 65 °C and stirred for 2 hours at the same temperature. Cooled to room temperature, added 100 mL of DI water to the RB and stirred overnight. Allowed the reaction mass to settle, decanted the supernatant, and washed the solid obtained with DI water repeatedly *via* centrifugation to remove excess acid content. Washings were continued until the pH of the supernatant solution became ~7. Dried the solid obtained at 80 °C overnight.

Ball milling of activated carbon with fine sand

We performed the ball milling of activated carbon with fine sand due to some specific pros associated with the process. Ball milling helps in reducing the particle size of both sand and carbon, resulting in very fine particles with increased surface area and hence active sites for adsorption. The mechanical energy of ball milling helps in the creation of pores and defects in the sand-carbon composite. These pores and defects act as adsorption sites. The ball milling results in a homogeneous mixture of these two components. This avoids the possible agglomeration of carbon particles and hence ensures high surface area of carbon is readily available for the adsorption process.

Ball milling was performed using the high-energy planetary ball mill available in our research centre. 30 g of fine sand and 3 g of activated carbon were taken in the stainless-steel milling vessel. Alumina balls of diameter 3 mm, 6 mm, and 20 mm in the ratio 50 : 30 : 4 was used as grinding media. The rotation speed was 150 rpm. Ball milling was carried out for a duration of 4 hours.

Strategy behind the selection of materials and a hybrid model of filtration

We employed some of the easily available, environmentally friendly and cost-effective adsorbents with some specific modifications and used them as components in our hybrid filtration setup. Sand, one of the naturally abundant materials, was collected, washed, dried and ball-milled to get fine sand. Compared to coarse sand, fine sand has better adsorption capacity due to its high specific surface area (~5 to 50 $m^2 g^{-1}$), reduced particle size (~0.1 to 10 μm) and pore size (~2 to 50 nm). This fine sand can well remove the suspended solids, organic particles like algae, coarse particles such as minerals and larger salts. Another material used was activated carbon, known as a universal adsorbent. It is one of the best-known materials for the adsorption process. It can adsorb a variety of organic matters such as hydrocarbons, pesticides, and volatile organic compounds. It can also trap some of the heavy metals to a small extent. The exceptional adsorption ability of activated carbon is attributed to its very high surface area (500 to 2000 $m^2 g^{-1}$), highly porous structure (average pore diameter of 1–4 nm), and high pore volume (0.2 to 1.2 $cm^3 g^{-1}$). Along with the activated carbon, functionalized activated carbon (f-AC) was also employed for the filtration process. The treatment with the acid mixture generates carboxyl, hydroxyl, carbonyl and sulfonic functional groups on its surface. Due to this, surface acidity and hydrophilicity increase. The creation of these negative functional groups on the surface favours the adsorption of cationic species. This results in improved adsorption of heavy metals, polar organic impurities, and some of the monovalent and divalent ions. The major components of the hybrid system, the contaminants they remove, and the mechanism of removal are represented in Fig. 4, which is given below.

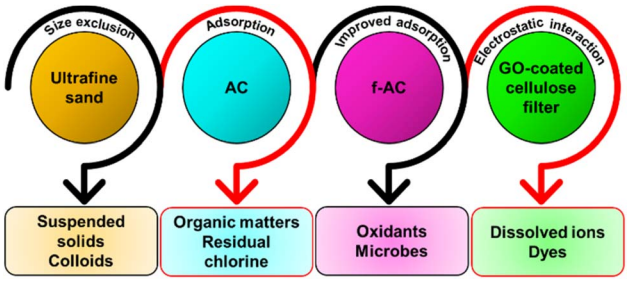

Fig. 4 Components of the hybrid filter with contaminants removed by them, along with the mechanism of removal.

Fabrication of hybrid filter and filtration of seawater

We developed our own hybrid filtration setup for the partial desalination of seawater, and its schematic representation is given in Fig. 5. Our multi-component filtration system consists of coated (GO/MXene) and uncoated cellulose filters, f-AC, ball-milled fine sand, and ball-milled sand with carbon.

We make use of a simple Buchner funnel for the construction of the hybrid filter. The porous base of the funnel was

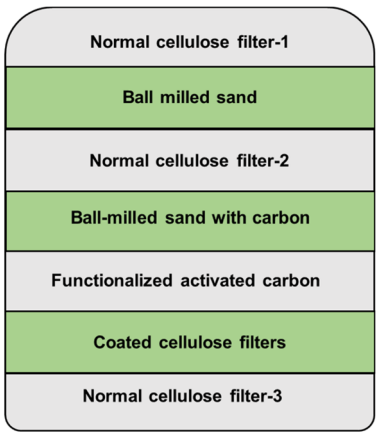

Fig. 5 Schematic representation of our hybrid filter with its various components.

covered by keeping a normal cellulose filter, followed by filters coated with 10 mL of GO solution of concentration 0.25 mg mL^{-1}. Then, thick layers of f-AC (5 g) and ball-milled sand-carbon were made (5 g). Subsequently, a normal cellulose filter, ball-milled fine sand layer (5 g), and another normal filter paper were placed at the top. Before filtering the actual seawater, roughly 1 L of DI water was passed through the filtration setup. This was to ensure the wetting of filter papers and the tight sealing of the components together. 200 mL of seawater was added dropwise to the filtration setup at a flow rate of ~2 L h^{-1} and allowed to pass through the hybrid filter without applying any external pressure. The collected seawater was passed through the same filter again for four more times. After that, the quality of seawater was analysed using salinity meter, total dissolved solid (TDS) meter, conductivity meter and pH meter. The coated filters and f-AC samples were recovered from the hybrid filter, dried at 50 °C for 4 hours, and analysed through FESEM with EDS. An exactly similar procedure was followed when three more GO-coated filters (0.50, 0.75 and 1 mg mL^{-1} solution coated) and four MXene-coated filters were used for the filtration. The highest concentration of coating solution was limited to 1 mg mL^{-1} so as to avoid the decrease in the water flux. The filter with the best result in both GO-coated and MXene-coated filters was taken for analysis.

Characterization techniques

The synthesized GO and $Ti_3C_2T_x$ MXene were characterized by XRD, FESEM, FTIR and UV-vis spectrometer. Powder X-ray diffraction (XRD) analysis was performed using a Rigaku D/MAX 2500 V diffractometer (Japan) equipped with Cu Kα radiation ($\lambda = 0.15498$ nm), operating at 40 kV and 100 mA. Scans were recorded over a 2θ range of 5° to 80° with a scanning speed of 5° per minute to investigate the crystal structure and characteristics of the synthesized GO and $Ti_3C_2T_x$ MXene. The surface morphology of GO, $Ti_3C_2T_x$ MXene, coated cellulose filters and f-AC was examined using a field emission scanning electron microscope (FESEM, Hitachi S-4800, Japan). UV-visible spectroscopy was conducted using a TU-1901 spectrophotometer (Persee) to obtain absorbance spectra for the materials. Functional groups on the surface of materials were characterized by Fourier-transform infrared (FTIR) spectroscopy using a PerkinElmer Spectrum 100 instrument, scanning the range from 4000 cm^{-1} to 400 cm^{-1}. Autosorb IQ-XR-XR, Anton Paar, Austria, instrument was employed for the calculation of the specific surface area of the f-AC sample before and after the filtration. The zeta potential of the GO-coated filter before and after filtration was measured using Anton Paar, surPASS 3 zeta potential analyzer. The quality of filtered seawater was tested using Equiptronics digital salinity meter (EQ-672), TDS meter (EQ-680), conductivity meter (EQ-664A), and pH meter (EQ-680).

Results and discussions

Characterization of GO

FESEM analysis. The surface morphology of the synthesised GO was analysed using FESEM at various magnifications, as illustrated in Fig. 6. The low magnification image (Fig. 6a) shows characteristic layered, flake-like, and wrinkled morphology with lateral dimensions varying between approximately 1–5 μm. The structure shows overlapped and loosely stacked layers, suggesting effective exfoliation and minimum agglomeration. The layers are partially stacked with definite spacing between them. The higher magnification image (Fig. 6b) displays distinct edges and surface folding, suggesting the flexibility of the material. These edges are irregular, typical in the case of chemically exfoliated GO.[24]

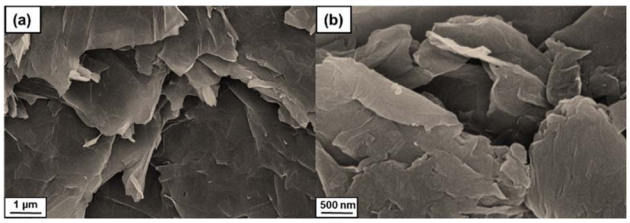

Fig. 6 FESEM images of synthesised GO at two different magnifications; lower magnification image showing the typical flake-like and layered morphology of GO sheets (a), and higher magnification image revealing wrinkled, thin sheets and loosely stacked structures (b).

XRD analysis. The XRD pattern of GO is given in Fig. 7a. A prominent diffraction peak is observed around an angle of 10.1° corresponding to the (001) plane. Whereas in the case of precursor graphite material, the most prominent peak is observed around 26°, corresponding to the (002) plane, which reflects a highly ordered stacked structure as discussed in the cited literature.[24,25] Due to the oxidation, this ordered nature is disrupted, and the formation of functional groups such as hydroxyl, epoxy, carboxylic, *etc.*, destroys the π–π stacking, resulting in the elimination of the (002) peak. The significant shift in the major peak towards the lower angle suggests that increased interlayer spacing due to the exfoliation of the layers. The calculated *d*-spacing using Bragg's equation was found to be 0.87 nm, which is considerably larger than the reported *d*-spacing value for the graphite (~0.35 nm).[24]

FTIR analysis. The presence of different oxygen-containing functional groups as a result of the oxidative treatment of graphite is confirmed by the GO's FTIR spectrum, which is shown in Fig. 7b. The presence of hydroxyl groups on the GO surface is indicated by a broad and intense signal at 3440 cm^{-1} that corresponds to the O–H stretching vibrations. The C=O stretching vibration of carbonyl groups, which were formed during the oxidation process, is responsible for the significant absorption at 1726 cm^{-1}. The C=C skeletal vibrations of unoxidized graphitic domains and epoxy (C–O–C) stretching vibrations are observed at 1601 cm^{-1} and 1200 cm^{-1}, respectively. Further oxidation and functionalization of the carbon framework are confirmed by the peak at 1034 cm^{-1} (C–O stretching). Finally, a band is observed at 866 cm^{-1}, arising from C–H out-of-plane bending vibrations. These detected functional groups suggest the existence of a variety of oxygenated moieties (–OH, C=O, C–O–C, and C–O) dispersed over both edge and basal sites and validate the successful oxidation

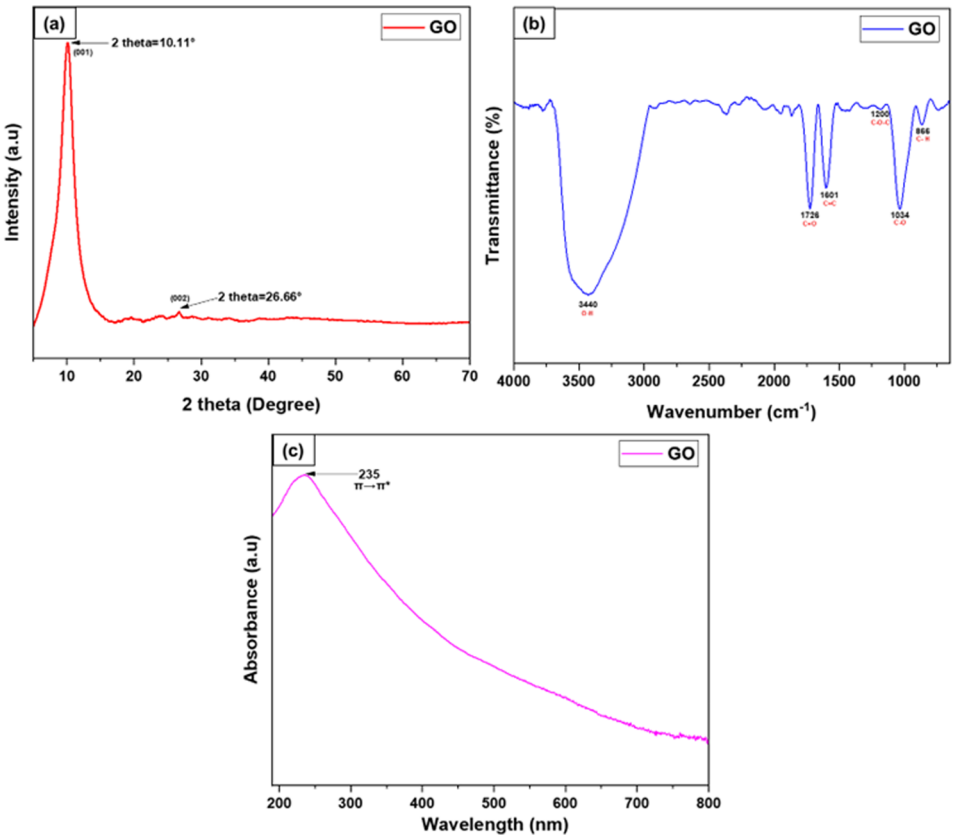

Fig. 7 The XRD pattern of the synthesised GO with a prominent peak at 10.11° (a), FTIR spectrum with oxygen-containing functional groups confirming the successful oxidation of graphite (b) and UV-vis spectrum showing a peak at 235 nm corresponding to the π → π* transition of C=C (c).

of graphite to graphene oxide. These surface features improve GO's hydrophilicity and dispersibility.[26,27]

UV-vis analysis. The UV-vis spectrum of the GO is represented in Fig. 7c. A sharp peak is observed at 235 nm, arising from the π → π* of aromatic C–C bonds, aligning with the other reported studies.[28] This peak indicates the presence of aromatic sp^2-hybridized domains of GO. The precursor natural graphite exhibits a strong peak around ~270 nm, suggesting a highly conjugated structure with no oxidation, as reported in the literature.[29] This peak in blue shifted to 235 nm in the case of GO, revealing the disruption of the conjugated structure due to oxidation.[30]

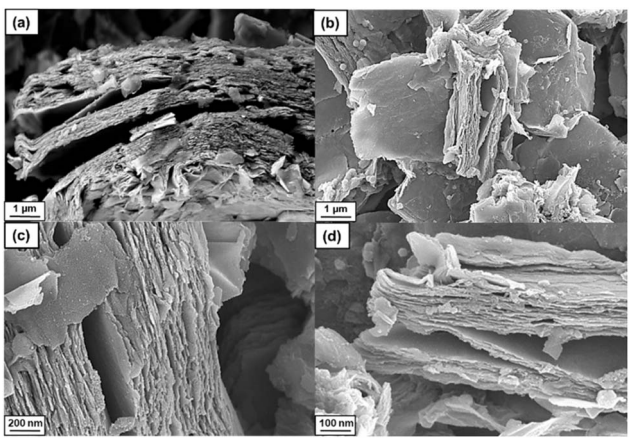

Fig. 8 FESEM images of $Ti_3C_2T_x$ MXene at lower (a and b) and higher magnifications (c and d) show typical accordion-like morphology with prominent, well-arranged layers. The smooth surface and irregular edges can be seen in the images.

Characterization of $Ti_3C_2T_x$ MXene

FESEM analysis. The low and high-magnification FESEM images of synthesised $Ti_3C_2T_x$ are given in Fig. 8. The well-defined layered-like morphology, similar to that of an accordion structure is seen in Fig. 8a and b. The images show multiple layers with prominent interlayer spacing, which suggests better etching and delamination of the precursor Ti_3AlC_2 MAX material. The higher magnification images reveal well-arranged layers with smooth surfaces (Fig. 8c and d). The edges seem to be irregular and fractured due to the exfoliation. The sharpness and distinct outlines of these edges suggest the thin flakes of a few-layered MXene sheets. These layers are orderly packed, indicating the preservation of structural integrity.[31,32]

XRD analysis. The XRD spectrum of the $Ti_3C_2T_x$ MXene synthesised *via* the HF etching method is given in Fig. 9a. The characteristic peaks are observed at a 2θ value of 6.3° (002), arising from the interlayer spacing between the MXene layers

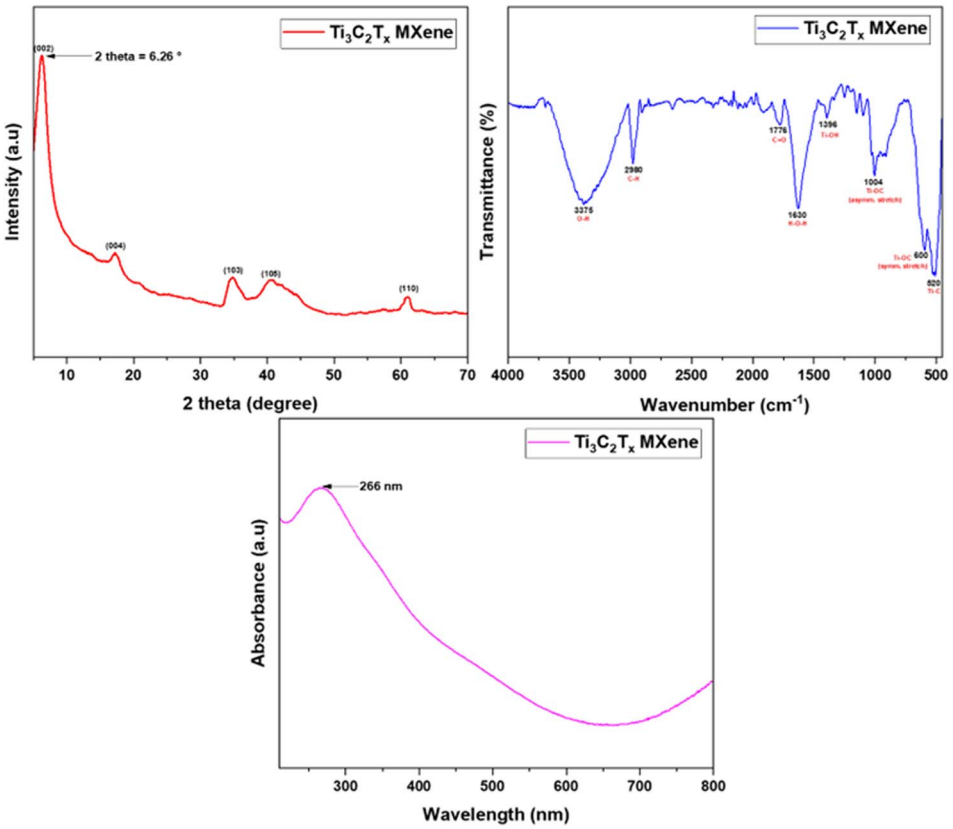

Fig. 9 The XRD pattern of $Ti_3C_2T_x$ MXene with relevant peaks (a), FTIR spectrum (b) and UV-vis spectrum (c) confirming the successful synthesis of MXene.

due to the surface terminations. The interlayer spacing was found to be 1.4 nm. This peak suggests the etching of Al layers from the Ti_3AlC_2 precursor. A weak peak was observed around 17.2° and assigned to the (004) plane, a second-order reflection from the (002) plane. The periodicity of the layers is confirmed by the presence of this particular peak.[33,34] Two more peaks are observed at around 35° and 40.7°. Since there are no peaks around 9°–10°, suggesting the proper etching of Al layers, these two observed peaks can be assigned as higher-order reflections from the MXene arising from (103) and (105) planes. These peaks are weak and broad when compared to the 6.3° peak, supporting that the origin is from higher-order reflections from the MXene. Another weak peak observed at 61° is assigned to the (110) plane of MXene. These observations support the successful synthesis of MXene from its precursor material.[33,34]

FTIR analysis. Fig. 9b illustrates the FTIR spectrum of $Ti_3C_2T_x$ MXene, which indicates the presence of structural vibrations and characteristic surface terminations that are the consequence of the etching and delamination processes. The O–H stretching vibration of surface hydroxyl groups and adsorbed water molecules is responsible for a broad absorption band focused at 3375 cm^{-1}. The peak at 2980 cm^{-1} is attributed to C–H stretching vibrations, which may be the result of residual organic species from synthesis. The absorption at 1776 cm^{-1} is indicative of the presence of terminal carbonyl groups on the surface, as it corresponds to C=O stretching vibrations. The presence of intercalated or adsorbed water within the MXene layers is confirmed by the peak observed at 1630 cm^{-1}, which is a result of H–O–H bending. Ti–OH bending vibrations, which are typical of surface hydroxyl terminations introduced during etching, are ascribed to a distinct peak at 1396 cm^{-1}. The Ti–OC bond elongation (asymmetric stretch) is indicated by a robust peak at 1004 cm^{-1}, which suggests partial oxidation and bonding between titanium and surface oxide groups. Usually, these asymmetric stretch vibrations are often associated with complementary symmetric modes at relatively lower wavenumbers. In the present case, this Ti–OC symmetric stretch mode is observed around 600 cm^{-1}. Finally, a peak around 520 cm^{-1} represents the Ti–C lattice mode vibration of the backbone. The successful synthesis of $Ti_3C_2T_x$ MXene is collectively confirmed by these vibrational features.[31,35]

UV analysis. The UV-vis spectrum of $Ti_3C_2T_x$ is represented in Fig. 9c. The spectrum shows a prominent peak around 266 nm, which is attributed to the interband transitions. These transitions usually involve the electronic band structure of the surface terminations of the MXene. $Ti_3C_2T_x$ MXenes exhibit metallic conductivity. In metals, UV-vis absorption is primarily governed by the excitation of electrons from occupied electronic states to unoccupied higher energy states, commonly known as interband transitions. $Ti_3C_2T_x$ MXenes are generally terminated with functional groups such as –O, –OH, and –F. These surface terminations considerably affect the electronic band structure

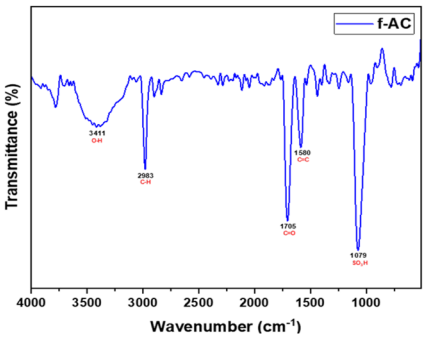

Fig. 10 FTIR spectrum of f-AC confirming the incorporation of various oxygen-containing functional groups onto it.

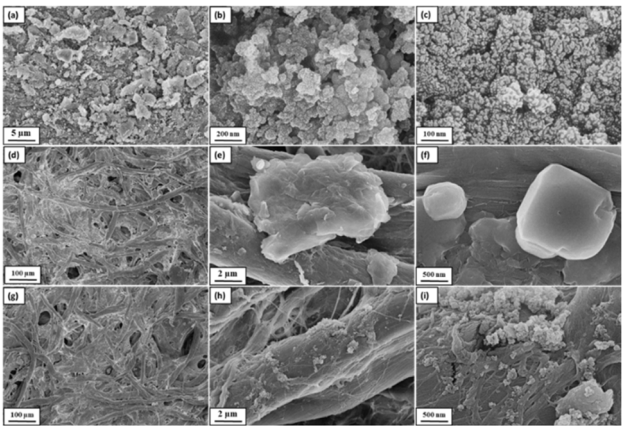

Fig. 11 Low and high magnification FESEM images of functionalized carbon show NaCl nanoclusters (a–c), GO-coated filter showing NaCl microcrystal formation (d–f) and $Ti_3C_2T_x$-coated filter with bigger nanoclusters (g–i).

and act as the origin for the above-mentioned peak in the spectrum. Along with this, a broad tailing is observed in the region of around 700–900 nm, which is attributed to the localised surface plasmon resonance.[36,37]

Characterization of f-AC by FTIR. The FTIR spectrum of f-AC, as illustrated in Fig. 10, exhibits several distinctive peaks that correspond to surface functional groups that have been introduced by acid modification using a H_2SO_4 + HNO_3 mixture. The stretching vibration of –OH is represented by a broad absorption band at 3411 cm^{-1}. The peak at 2983 cm^{-1} is attributed to C–H stretching vibrations, which suggest the presence of aliphatic hydrocarbon chains or residual organic groups on the carbon surface. The presence of carboxylic acid is suggested by the prominent and sharp peak observed at 1705 cm^{-1}, which is indicative of C=O stretching vibrations. The partially conjugated structure of carbon and its surface oxidation are reflected in another intense peak at 1580 cm^{-1}, which is attributed to the stretching of aromatic C=C bonds. The presence of a peak at 1079 cm^{-1} is attributed to C–O stretching vibrations, which are typically derived from alcohols or ethers. By introducing a variety of oxygenated groups, including –OH, –COOH, and C=O, the acid treatment has efficiently functionalized the activated carbon surface, thereby increasing the material's acidity and adsorption potential.[38–40]

Characterization of carbon and coated filter after the filtration of seawater

The carbon samples and coated filters used for the filtration of seawater were analysed using FESEM with EDS to study their morphology and elemental analysis. In both GO-coated and $Ti_3C_2T_x$-coated filters, the filters coated with 1 mg mL^{-1} solution were found to be giving better results than the others and hence considered for the analysis.

FESEM analysis. The FESEM images of f-AC and coated filters after the seawater filtration are given in Fig. 11. The low and high-magnification images of f-AC after the filtration are given in Fig. 11a–c. The images show a rough and highly porous surface morphology with an agglomerated structure, typical of that of other studies.[38,39] Since we have employed an H_2SO_4 + HNO_3 acid mixture for the treatment of carbon, this kind of morphology is expected. The treatment with acid helps in increasing the surface area, etching the surface, and introducing functional groups such as –COOH, –OH or $–SO_3H$. This leads to a disordered and amorphous surface texture. The enhanced roughness and heterogeneity improve the material's adsorption capacity, especially for ionic species. Also, acid treatment eliminates contaminants and opens micropores and mesopores, facilitating the process of adsorption.

It is evident from the images that there are several light-coloured regions (white shades) which are well dispersed across the carbon surface. These are the crystalline NaCl deposits that have adhered to the carbon substrate. In the case of FESEM images, the dense regions, such as salts or heavier elements, usually appear brighter due to the increased backscattering of electrons.[41] The proper distribution of these white shades throughout the carbon surface is evidence of the effective interaction between the NaCl present in the seawater and the functionalized porous carbon surface. The acid treatment introduces oxygen-bearing functional groups on the surface of carbon. These groups ionise in water and make the surface negatively charged.[42,43] The positively charged Na^+ ions present in the seawater get electrostatically attracted towards these negatively charged surfaces.[44] The local accumulation of these Na^+ ions results in an electrical double layer. The adsorption of only Na^+ ions leads to the development of excessive surface charge, which is energetically unfavourable.[45] So, the system seeks electrochemical balance and hence to maintain electrical neutrality, the negatively charged Cl^- ions present in the water start to diffuse towards the electrical double layer. This leads to a high local concentration of both ions, leading to nucleation and growth of NaCl nanocrystals, followed by nanoclusters, especially as water evaporates or after drying the carbon sample.[45]

The different magnification FESEM images of the GO-coated filter after the filtration of seawater are presented in Fig. 11d–f. The fibrous network of cellulose fibres is clearly visible as seen in the case of Fig. 11d. The individual fibres appear cylindrical and their diameter varies slightly, ranging from 10–20 µm.[46] The fibres show a rough surface texture due to their surface porosity.

The fibrous network seems to be highly entangled, leading to a nonwoven mesh-like structure. This entanglement helps in mechanical strength, controlling porosity and permeability. The dark regions present in the image represent the voids between the fibres, resulting from inter-fibre pores which are irregular in shape and size.[47] The GO coating can be seen as a layer or film-like substance covering the cellulose fibres. The adhesion of GO onto the fibrous network can be seen clearly in Fig. 11e. The GO sheets look wrinkled and overlapping associated with edges and folds owing to the lamellar and flexible nature of GO.[48] The GO sheets are well-adhered to the surface of the cellulose fibre due to the hydrogen bonding between the functional groups on the GO and cellulose surfaces.[49] The oxygen-containing functional groups, such as hydroxyl (–OH), carboxyl (–COOH), and epoxy (–O–) are abundant on the surface of GO. The presence of these groups enhances the hydrophilicity of the GO and hence facilitates its better interaction with water and dissolved ions. The high surface area of GO ensures numerous sites for interaction and adsorption of ions. The mechanism of ion adsorption in the case of the GO-coated filter is quite similar to that of f-AC as discussed earlier. The positively charged Na^+ ions are getting electrostatically attracted towards the negatively charged functional groups present on the surface of GO, leading to the formation of an electrical double layer. Consequently, the Cl^- ions start to move towards these electrical double layers to maintain electrical neutrality, leading to the local accumulation of both ions. In the case of FESEM images of f-AC, we observed the formation of NaCl nanoclusters, but when it comes to the images of GO-coated filters, NaCl crystals were observed with lateral sizes ranging from 0.5–3 μm (Fig. 11f). The above-mentioned pathway of NaCl adsorption on the surface of GO-coated filter is schematically represented in Fig. 12. When we consider the $Ti_3C_2T_x$-coated filter after the filtration, NaCl nanoclusters were observed as in the case of f-AC, but the clusters seemed to be bigger. In the case of MXene, the surface is decorated with –OH, and –F terminal groups due to the HF etching and delamination process.[35] This results in a strong negatively charged surface which attracts the dissolved Na^+ ions and hence the consequent adsorption processes to be followed as discussed above.

The difference in the morphology of adsorbed NaCl is a result of the variation in surface chemistry, ion mobility, and nucleation behaviour among the materials. A dense network of nucleation sites is provided by f-AC, which is characterized by a porous structure that is rich in oxygen-containing functional groups.[50] The mobility of hydrated ions can be restricted by the predominance of micropores in f-AC, despite its high surface area. This results in a uniformly distributed NaCl nanocluster and a restriction of the extent of crystal growth.[51] Conversely, the GO-coated filter exhibits a surface that is relatively flat and less geometrically porous. The kinetics of stable nucleation may be influenced by the specific nature of these sites and the smooth surface characteristics, allowing for more extensive lateral ion migration across the GO surface, despite the fact that the GO surface is rich in oxygen-containing functional groups that provide abundant potential interaction sites.[52] Moreover, the substantial delay in water evaporation during the post-filtration drying process is facilitated by the strong hydrophilicity of GO,[52] which promotes the formation of fewer but larger, micron-sized NaCl crystals. Filters coated with $Ti_3C_2T_x$ MXene demonstrate a surface that is moderately hydrophilic and contains functional groups that are capable of adsorbing Na^+ ions.[35] Nucleation is facilitated by the effective ion–surface interactions on MXene, which results in the formation of nanoclusters.[53] The clusters on $Ti_3C_2T_x$ are larger than those on f-AC, despite remaining confined to the nanoscale, as a result of its moderate ion mobility and lower porosity in comparison to f-AC. The general mechanism of cation adsorption by the negatively charged surface terminations of GO is given in Fig. 12.

EDS analysis. The elemental composition, quantification, and mapping of f-AC, GO-coated filters, and $Ti_3C_2T_x$-coated filters after filtration were examined using EDS, as shown in Fig. 13. For f-AC (Fig. 13a–c), it indicates that C and O dominate due to their oxidised carbon nature. Significant amounts of Na, Cl, S, and Ca are also present. The clear detection of Na and Cl confirms efficient salt adsorption, while the presence of sulphate and trace of Ca indicates additional ion trapping. Similarly, the GO-coated filter (Fig. 13d–f) shows substantial Na and Cl capture, consistent with FESEM observations and highlighting its strong salt adsorption capability. Results for the $Ti_3C_2T_x$-coated filter (Fig. 13g–i) also show Na and Cl, confirming salt trapping, but at lower quantities than the other two

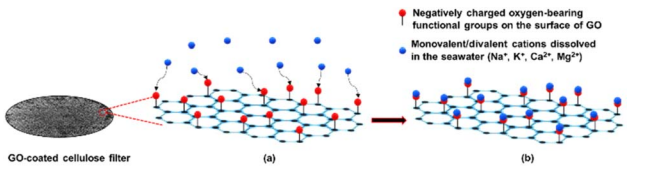

Fig. 12 The general pathway for cation adsorption leading to salt removal by the negatively charged surface of the GO-coated cellulose filter. Electrostatic attraction of positively charged ions dissolved in seawater towards the negatively charged surface terminations of GO (a) and their trapping onto the surface (b).

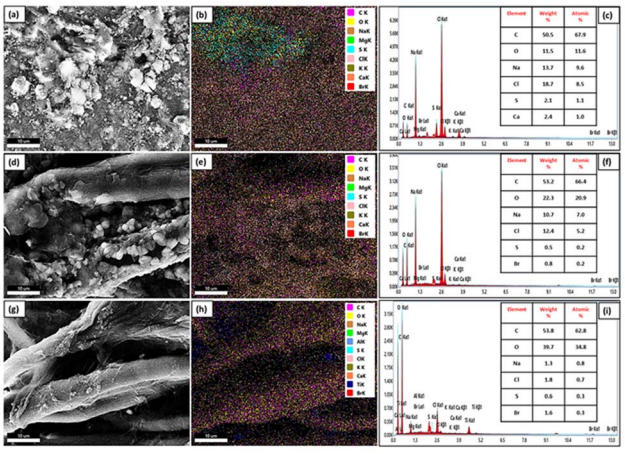

Fig. 13 The selected FESEM image for EDS analysis, total elemental mapping, and EDS spectra of f-AC (a–c), GO-coated filter (d–f) and $Ti_3C_2T_x$-coated filter (g–i) proves the adsorption of salt from all three with different extents.

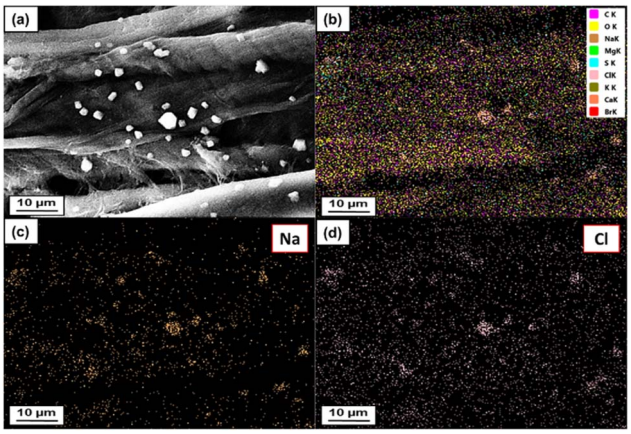

Fig. 14 FESEM image of a specific region of the GO-coated filter containing microcrystals (a), its complete elemental mapping (b), individual mapping of Na (c) and Cl (d) confirming the formation of NaCl microcrystals.

materials. This suggests moderate adsorption efficiency. Although MXene is promising for desalination, its performance is reduced in passive filtration compared to ion-intercalation-based approaches such as capacitive deionisation. The superior Na and Cl uptake of GO is attributed to its abundant oxygen functional groups and accessible surface area, while $Ti_3C_2T_x$ may experience restacking and limited surface interaction under passive conditions, reducing ion uptake.

The formation of NaCl microcrystals on the GO-coated filter was confirmed through EDS analysis of a crystal-rich region, as shown in Fig. 14. The FESEM image (Fig. 14a) clearly displays the salt crystals. Complete elemental mapping is provided in Fig. 14b, while individual Na and Cl maps are shown in Fig. 14c and d, respectively. Both elements appear in high concentrations at the exact locations of the observed crystals, confirming that the detected microcrystals are NaCl.

BET surface area analysis of f-AC. The f-AC used in the hybrid filter was analysed using BET to determine the specific surface area (SSA) of the sample before and after the filtration of seawater. The N_2 adsorption–desorption isotherm plots and surface area plot for the f-AC before filtration are given in Fig. 15a and b. The curve exhibits a Type IV isotherm with a hysteresis loop, which is a characteristic of mesoporous materials (Fig. 15a).[54] A low N_2 uptake at relatively low P/P_0 indicates the limited microporosity, while the observed steep rise at higher P/P_0 suggests the capillary condensation. The SSA was calculated using the multi-point BET method (Fig. 15b). After extracting a linear plot having 5 points ranging from $0.05 < P/P_0 < 0.30$ (correlation coefficient, $r = 0.996919$), the calculated value of SSA for the f-AC was found to be 384.621 $m^2\ g^{-1}$. This high value indicates a highly porous structure containing abundant sites for adsorption. After filtration of the seawater, the isotherm curve of the f-AC still follows type IV, but the adsorption has been reduced significantly (Fig. 15c). The calculated SSA for this sample was found to be just 36.754 $m^2\ g^{-1}$ (Fig. 15d). This substantial reduction in SSA is evidence of the claim that f-AC has successfully trapped ions and other impurities from the seawater in the present work.

Zeta potential analysis of GO-coated filter. Zeta potential measurements were conducted to investigate how the surface charge of the GO-coated filter changes before and after seawater filtration (Fig. 16). The pristine GO-coated filter exhibited a zeta potential of -7.7 ± 0.5 mV, indicating its naturally negative surface charge due to oxygen-containing groups such as carboxyl, hydroxyl, and epoxy functionalities on the GO sheets.[55] After filtration of seawater, the zeta potential shifted to -2.02 ± 0.3 mV, demonstrating a notable reduction in surface charge magnitude. This decrease is attributed to the adsorption of positively charged ions (predominantly Na^+) from seawater onto the GO surface, which leads to compression of the electrical double layer and partial neutralization of the negative surface sites. This change in surface potential confirms that electrostatic interactions play a significant role in the interaction between negatively charged GO surface and positively charged ions dissolved in the seawater.[56] The observation aligns with classical electrical double-layer theory, where counterions accumulate near charged surfaces and reduce the measured potential through charge screening.[57,58] Overall, the zeta

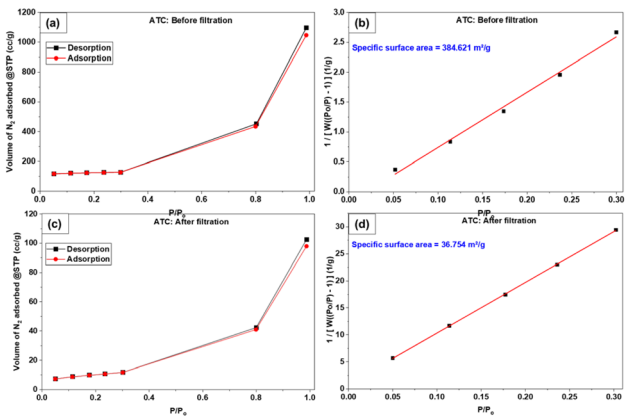

Fig. 15 The N_2 adsorption–desorption isotherms and BET plots of the f-AC before (a and b) and after (c and d) seawater filtration. The decreased SSA from 384.621 $m^2\ g^{-1}$ to 36.754 $m^2\ g^{-1}$ after filtration of seawater indicates pore blockage and salt deposition.

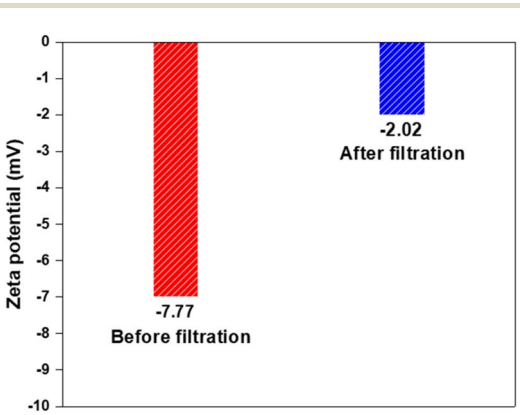

Fig. 16 Zeta potential analysis of the GO-coated filter before and after filtration of seawater, showing a shift in zeta potential from −7.7 mV to −2.2 mV after the filtration due to the adsorption of cations from the negatively charged GO surface.

potential results provide direct evidence that cation adsorption on the GO surface is primarily driven by electrostatic forces during the filtration process.

Evaluation of pre-treatment performance. The seawater after filtration through the hybrid filter was analysed using various water quality tests. The GO-coated filter with a 1 mg mL^{-1} concentrated solution displayed the best result when compared to the rest of the setups. The total suspended solids (TSS) of the filtered water were estimated as 8.0 mg L^{-1}. The value of total colloids was found to be 1.8 Nephelometric Turbidity Unit (NTU), while the total hardness was 185 mg L^{-1} ($CaCO_3$ equivalents). The microbial quality of pretreated seawater was assessed using the most probable number (MPN) method, yielding a count of 27 coliforms per 100 mL. The above-mentioned tests were performed under the guidelines of the Food Safety and Standards Authority of India, Government of India. The chemical oxygen demand (COD) value of the water sample was found to be 4.2 mg L^{-1}, whereas the biochemical oxygen demand (BOD) was 1.1 mg L^{-1}. The turbidity was measured using the nephelometric method (APHA 2130 B), and the value was found to be 0.6 NTU. The silt density index (SDI), which is a vital parameter to test the quality of feedwater for commercial RO desalination plants, was calculated using ASTM D4189-07(2014) guidelines. The SDI value was found to be 2.6, which is an acceptable value.

The efficient operation of the gravity-driven hybrid filter in enhancing seawater quality is due to the synergistic function of its sequential components: fine sand, activated carbon, f-AC, and GO-coated cellulose filter paper. Each layer served a unique function in eliminating particular categories of contaminants, together aiding in the decrease of turbidity, suspended particles, microbial load, and organic matter. Fine sand, functioning as the initial layer, largely served as a mechanical barrier that trapped large particle matter and debris by size exclusion. This phase helped in diminishing turbidity and TSS, hence enhancing the efficiency of the next filtering stages. Activated carbon, ball-milled with fine sand, offers an extensive surface area with a porous configuration, optimal for the adsorption of organic chemicals and trace metals. It also performed a vital function in odour elimination and diminishing colour resulting from dissolved organics. This layer facilitated the noted decrease in COD and BOD. The f-AC showed better removal efficiency due to the incorporation of oxygen-containing functional groups, which enhanced surface polarity and affinity for polar pollutants. These adjustments enhanced the adsorption of low molecular weight organics, metal ions, and microbial pieces, hence facilitating the reduction in COD and microbial count. Finally, a cellulose filter paper coated with GO functioned as a nano-engineered membrane providing size-based exclusion and electrostatic interactions. GO possesses negatively charged oxygenated functional groups that facilitate the entrapment of bacteria and colloids through electrostatic attraction, elucidating the low MPN value and colloidal concentration. Moreover, its fine structure facilitated the elimination of residual turbidity and ultrafine suspended particles.

Traditional seawater pretreatment techniques such as multimedia filtration (MMF), ultrafiltration (UF), and chemical dosing require external power, proper infrastructure, and significant operational expenses. In contrast, the gravity-driven hybrid filter presented in this study provides a low-energy, cost-effective alternative that does not compromise performance. MMFs are successful at reducing turbidity and TSS, however, they have limitations in removing dissolved organics and microorganisms. The proposed system outperforms this by combining activated carbon and functionalized carbon to adsorb organic molecules, resulting in low COD (4.2 mg L^{-1}) and BOD (1.1 mg L^{-1}). UF membranes provide good microbiological and fine particle removal, but they require high pressure, regular maintenance, and are prone to fouling. The hybrid filter's GO-coated cellulose layer matches UF performance in a passive system, with turbidity of 0.6 NTU and microbiological counts of 27 MPN/100 mL in the absence of applied pressure. Most importantly, the technique eliminates chemical additives, lowering the risk. The performance of the present work has been compared with other similar works and represented in Table S2 (see SI) for detailed comparison. Overall, this hybrid filter provides a sustainable and efficient alternative to conventional systems. Despite this passive operation, the system excels at contaminant removal due to the synergistic physical, chemical, and electrostatic actions of its hybrid materials. The high quality of the treated seawater makes it an excellent feedwater for the commercial desalination plants, showcasing a sustainable and scalable approach for seawater pretreatment. The filter has a strong potential for scalability due to its low cost, simple design, and zero energy requirement. The use of readily available materials and the minimum usage of GO help in achieving cost-effectiveness. Even though some parameters have a value slightly higher than the RO pretreatment standards, we believe that by constructing a compact device with multiple hybrid filters and applying a minimum amount of external pressure can solve this issue effectively.

Evaluation of desalination performance. All 8 water samples filtered through hybrid filters were analysed using pH meter, TDS meter, conductivity meter and salinity meter. The values corresponding to these parameters are given in Table S3 (see SI). The unfiltered seawater was found to have a pH of 7.97, a TDS of 34.7 PPT, a conductivity of 48.01 mS cm^{-1} and a salinity of 34.4 parts per thousand (PPT). Among the filtered samples, the comparatively best results were obtained when 1 mg mL^{-1} GO-coated filters were used in the hybrid setup. This particular sample displayed pH, TDS, conductivity and salinity values of 7.10, 29.1 PPT, 42.47 mS cm^{-1} and 28.3 PPT, respectively, with a total decrease in salinity of 17.7%. It was observed that, in the case of both GO and MXene-coated filters, desalination performance was found to be increased with an increase in the concentration of the coating solution from 0.25 mg mL^{-1} to 1.0 mg mL^{-1}. An increase in GO/MXene concentration enhances salt removal efficiency by providing a higher density of negatively charged functional groups such as carboxyl and hydroxyl, which attract and bind positively charged ions like Na^+, Ca^{2+}, and Mg^{2+}. Additionally, higher loading results in a denser coating with reduced pore size and increased surface area, allowing for better electrostatic interaction, physical trapping, and slower ion passage. These combined effects lead

Table 1 Concentration of major ions in seawater before and after filtration

Ions	Quantity (mg L^{-1})		
	Before filtration	After filtration	Reduction (%)
Na^+	10 212	8545	16.3
Ca^{2+}	529	424	19.8
Mg^{2+}	1278	991	22.4
K^+	345	288	16.5
Cl^-	19 200	16 750	12.8
PO_4^{3-}	11.932	5.147	56.9
SO_4^{2-}	2361	2069	12.4

to more effective salinity reduction, even under passive, gravity-driven filtration conditions.

Based on the above results, the seawater filtered through the hybrid filter containing 1.0 mg mL^{-1} GO-coated filters was tested for the determination of various elements using the guidelines provided by the Bureau of Indian Standards, Govt. of India and the data is provided in Table 1.

The above results suggest that the presented hybrid approach is effective in dual functioning; impressive pretreatment, and partial desalination. Even though the salinity was reduced to 28.3 PPT from 34.4 PPT (17.7% reduction), this water cannot be used anywhere directly. However, by combining the multiple filters or increasing the thickness of the adsorbent layers in the hybrid filter, still better results can be achieved without any external energy supply. The simplicity in operation, the eco-friendly materials used, and the zero external energy input for the filtration in the proposed approach contribute to the sustainable solutions for the water crisis management.

Conclusion

The present study demonstrates an effective, eco-friendly, and energy-efficient approach for the effective pretreatment followed by partial desalination of seawater using a gravity-driven hybrid filtration system. By employing naturally available materials such as fine sand, carbon, and cellulose, combined with nanomaterial coatings of GO and $Ti_3C_2T_x$ MXene, a multi-layered filter was fabricated in a sandwich structure that facilitates filtration without the need for external pressure or energy input. This not only simplifies the operation but also enhances the sustainability of the system. The fabricated filter was able to treat up to 2 litres of seawater per hour with a minimal filtration area of approximately 63 cm^2, showcasing the scalability and practicality of the design. Systematic evaluation of different coating concentrations revealed that a 1 mg mL^{-1} solution provided the most effective salt rejection performance for both GO and MXene. However, the GO-coated filter demonstrated superior results, achieving a 17.7% reduction in salinity. This performance is primarily attributed to the adsorption capability and electrostatic interactions between the negatively charged filter surfaces and dissolved ions in seawater. The findings indicate the potential of such gravity-based filtration systems for use as pre-treatment methods for commercial desalination plants to minimise overall energy consumption and membrane fouling issues in the case of membrane-based technologies.

Author contributions

M. M. D.: investigation, methodology, data curation, formal analysis, writing-original draft, writing – review & editing. A. B. S.: data curation, investigation. S. S.: data curation, writing-original draft. A. H. S.: formal analysis. N. W.: data curation, writing, S. K. T.: conceptualization, resources, supervision, funding acquisition, supervision, validation, writing – review & editing.

Conflicts of interest

There are no conflicts to declare.

Data availability

Raw data supporting the microscopic and spectroscopic results presented in this article are available from the corresponding author upon reasonable request.

The data supporting this article have been included as part of the supplementary information (SI). Supplementary information: comparison table of commercially available seawater pretreatment methods with the present study, a comparison table with various filtration-based pretreatment methods with the present study and one more table having seawater quality parameters values before and after the filtration through different set of hybrid filters. See DOI: https://doi.org/10.1039/d5na00691k.

Acknowledgements

SKT sincerely appreciate the support of the SPARC project (P3808) under the Indo-UK scheme. Additionally, SKT extends heartfelt gratitude to Nitte Deemed to be University for providing the research grant (Grant No. NUFR-23-070), which has significantly facilitated our research endeavours. SKT wholeheartedly thank the RSC *Nanoscale Advances* for publising this article without any APC.

References

1 M. A. Hanjra and M. E. Qureshi, *Food Policy*, 2010, **35**, 365–377.
2 V. Srinivasan, E. F. Lambin, S. M. Gorelick, B. H. Thompson and S. Rozelle, *Water Resour. Res.*, 2012, **48**, 2011WR011087.
3 H. Shemer, S. Wald and R. Semiat, *Membranes*, 2023, **13**, 612.
4 M. Elimelech and W. A. Phillip, *Science*, 2011, **333**, 712–717.
5 A. Subramani and J. G. Jacangelo, *Water Res.*, 2015, **75**, 164–187.
6 *Seawater Desalination: Conventional and Renewable Energy Processes*, ed. G. Micale, L. Rizzuti and A. Cipollina, Springer Berlin Heidelberg, Berlin, Heidelberg, 2009.

7 M. S. Islam, A. Sultana, A. H. M. Saadat, M. S. Islam, M. Shammi and M. K. Uddin, *J. Sci. Res.*, 2018, **10**, 77–97.
8 J. Feria-Díaz, M. López-Méndez, J. Rodríguez-Miranda, L. Sandoval-Herazo and F. Correa-Mahecha, *Processes*, 2021, **9**, 262.
9 L. F. Greenlee, D. F. Lawler, B. D. Freeman, B. Marrot and P. Moulin, *Water Res.*, 2009, **43**, 2317–2348.
10 A. Abushawish, I. Bouaziz, I. W. Almanassra, M. M. AL-Rajabi, L. Jaber, A. K. A. Khalil, M. S. Takriff, T. Laoui, A. Shanableh, M. A. Atieh and A. Chatla, *Water*, 2023, **15**, 1572.
11 L. Henthorne and B. Boysen, *Desalination*, 2015, **356**, 129–139.
12 N. Prihasto, Q.-F. Liu and S.-H. Kim, *Desalination*, 2009, **249**, 308–316.
13 M. Zeng, M. Chen, D. Huang, S. Lei, X. Zhang, L. Wang and Z. Cheng, *Mater. Horiz.*, 2021, **8**, 758–802.
14 S. Dervin, D. D. Dionysiou and S. C. Pillai, *Nanoscale*, 2016, **8**, 15115–15131.
15 M. M. Devadiga, A. S. Bhat, S. Rudra, N. Wang, G. C. Nayak and S. K. Tiwari, *ACS Appl. Eng. Mater.*, 2025, **3**, 3111–3126.
16 H. Li, H. Lin, S. Raza, Z. Zhao, S. Chen, Y. Wang, Q. Zeng, C. Chen, W. Yu and L. Shen, *Water Res.*, 2025, **286**, 124296.
17 Q. Zeng, X. Zhou, L. Shen, D. L. Zhao, N. Kong, Y. Li, X. Qiu, C. Chen, J. Teng, Y. Xu and H. Lin, *J. Membr. Sci.*, 2024, **700**, 122691.
18 H. Li, H. Lin, S. Raza, C. Chen, W. Yu, Q. Zeng, Z. Zhao, X. Huang and L. Shen, *J. Membr. Sci.*, 2025, **718**, 123685.
19 B. Wang, L. Shen, J. Xu, Z. Yang, Y. Chen, S. Chen, B. Li, C. Chen and H. Lin, *Sep. Purif. Technol.*, 2025, **356**, 129928.
20 L. Ranieri, R. E. Putri, N. Farhat, J. S. Vrouwenvelder and L. Fortunato, *Desalination*, 2023, **549**, 116353.
21 D. C. Marcano, D. V. Kosynkin, J. M. Berlin, A. Sinitskii, Z. Sun, A. Slesarev, L. B. Alemany, W. Lu and J. M. Tour, *ACS Nano*, 2010, **4**, 4806–4814.
22 D. C. Marcano, D. V. Kosynkin, J. M. Berlin, A. Sinitskii, Z. Sun, A. S. Slesarev, L. B. Alemany, W. Lu and J. M. Tour, *ACS Nano*, 2018, **12**, 2078.
23 M. Alhabeb, K. Maleski, B. Anasori, P. Lelyukh, L. Clark, S. Sin and Y. Gogotsi, *Chem. Mater.*, 2017, **29**, 7633–7644.
24 B. Paulchamy, G. Arthi and B. D. Lignesh, *J. Nanomed. Nanotechnol.*, 2015, **6**, 1.
25 S. Li, X. Lu, Y. Xue, J. Lei, T. Zheng and C. Wang, *PLoS One*, 2012, **7**, e43328.
26 T. F. Emiru and D. W. Ayele, *Egypt. J. Basic Appl. Sci.*, 2017, **4**, 74–79.
27 Y. Gong, D. Li, Q. Fu and C. Pan, *Prog. Nat. Sci.:Mater. Int.*, 2015, **25**, 379–385.
28 N. Pan, D. Guan, T. He, R. Wang, I. Wyman, Y. Jin and C. Xia, *J. Radioanal. Nucl. Chem.*, 2013, **298**, 1999–2008.
29 R. A. Senthil, A. Selvi, P. Arunachalam, L. S. Amudha, J. Madhavan and A. M. Al-Mayouf, *J. Mater. Sci.: Mater. Electron.*, 2017, **28**, 10081–10091.
30 V. C. Pham, Functional Graphene: Synthesis, Characterization and Application in Optoelectronics, Doctoral dissertation, Albert-Ludwigs-Universität Freiburg, 2015.
31 E. Lee, A. VahidMohammadi, B. C. Prorok, Y. S. Yoon, M. Beidaghi and D.-J. Kim, *ACS Appl. Mater. Interfaces*, 2017, **9**, 37184–37190.
32 Z. Li, L. Wang, D. Sun, Y. Zhang, B. Liu, Q. Hu and A. Zhou, *Mater. Sci. Eng., B*, 2015, **191**, 33–40.
33 L. Nguyen, A. Ali, S. Teke, R. M. Bhattarai, A. Denra, O. Q. Vu and Y. S. Mok, *Nanoscale Adv.*, 2025, **7**, 5313–5322.
34 J. Zhang, S. Tang, N. Ding, P. Ma and Z. Zhang, *Nanoscale Adv.*, 2023, **5**, 2921–2932.
35 F. Zhang, W. Liu, S. Wang, C. Liu, H. Shi, L. Liang and K. Pi, *Composites, Part B*, 2021, **217**, 108900.
36 T. S. Mathis, K. Maleski, A. Goad, A. Sarycheva, M. Anayee, A. C. Foucher, K. Hantanasirisakul, C. E. Shuck, E. A. Stach and Y. Gogotsi, *ACS Nano*, 2021, **15**, 6420–6429.
37 L. Chen, X. Ye, S. Chen, L. Ma, Z. Wang, Q. Wang, N. Hua, X. Xiao, S. Cai and X. Liu, *Ceram. Int.*, 2020, **46**, 25895–25904.
38 A. Allwar, R. Hartati and I. Fatimah, *AIP Conf. Proc.*, 2017, **1823**, 1.
39 P. Azhagapillai, A. Al Shoaibi and S. Chandrasekar, *Carbon Lett.*, 2021, **31**, 419–426.
40 J. L. Figueiredo, M. F. R. Pereira, M. M. A. Freitas and J. J. M. Órfão, *Carbon*, 1999, **37**, 1379–1389.
41 *Materials Characterization Using Nondestructive Evaluation (NDE) Methods*, Elsevier, 2016, pp. 17–43.
42 J. Zhou, P. Yang, P. A. Kots, M. Cohen, Y. Chen, C. M. Quinn, *et al.*, *Nat. Commun.*, 2023, **14**, 2293.
43 H. Peng, L. Dong, S. Gao and Z. Wang, *RSC Adv.*, 2022, **12**, 4475–4483.
44 A. Kumar and D. W. Chang, *Polymers*, 2024, **17**, 29.
45 A. R. Finney and M. Salvalaglio, *Faraday Discuss.*, 2024, **249**, 334–362.
46 D. O. Bokov, M. Z. Mahmoud, G. Widjaja, W. Suksatan, S. Chupradit, U. S. Altimari, H. A. Hussein, Y. F. Mustafa and M. Kazemnejadi, *RSC Adv.*, 2022, **12**, 10933–10949.
47 *Advanced Functional Materials and Sensors*, Springer Singapore, Singapore, 2019, pp. 7–28.
48 N. Kumar, B. Kumar, H. Gupta and A. Kumar, *Polymers*, 2023, **15**, 572.
49 X. Liu, T. Zhang, K. Pang, Y. Duan and J. Zhang, *RSC Adv.*, 2016, **6**, 73358–73364.
50 S. Liu, H. Wang, P. Neumann, C. S. Kim and K. J. Smith, *ACS Omega*, 2019, **4**, 6050–6058.
51 J. Desarnaud, H. Derluyn, J. Carmeliet, D. Bonn and N. Shahidzadeh, *J. Phys. Chem. Lett.*, 2014, **5**, 890–895.
52 D. R. Dreyer, S. Park, C. W. Bielawski and R. S. Ruoff, *Chem. Soc. Rev.*, 2010, **39**, 228–240.
53 C. E. Ren, K. B. Hatzell, M. Alhabeb, Z. Ling, K. A. Mahmoud and Y. Gogotsi, *J. Phys. Chem. Lett.*, 2015, **6**, 4026–4031.
54 C. Li, S. Zhao, M. Li, Z. Yao, Y. Li, C. Zhu, S.-M. Xu, J. Li and J. Yu, *Front. Environ. Sci.*, 2023, **11**, 976113.
55 S. M. Beladi-Mousavi, S. Sadaf, L. Walder, M. Gallei, C. Rüttiger, S. Eigler and C. E. Halbig, *Adv. Energy Mater.*, 2016, **6**, 1600108.
56 F. Baskoro, C.-B. Wong, S. R. Kumar, C.-W. Chang, C.-H. Chen, D. W. Chen and S. J. Lue, *J. Membr. Sci.*, 2018, **554**, 253–263.
57 K. Yang, B. Chen, X. Zhu and B. Xing, *Environ. Sci. Technol.*, 2016, **50**, 11066–11075.
58 S. K. Tiwary, M. Singh, S. V. Chavan and A. Karim, *npj 2D Mater. Appl.*, 2024, **8**, 27.